Geometric Conformity Assessment of a VPP-Manufactured Toroidal Propeller Using Optical 3D Scanning

Van Dong Pham (vandong.pham@unob.cz)[1], Dalibor Rozehnal (dalibor.rozehnal@unob.cz)[1], Vladimír Horák (vladimir.horak@unob.cz)[2]

[1] Department of Aviation Technology, University of Defence, Brno, Czech Republic
[2] Department of Mechanical Engineering, University of Defence, Brno, Czech Republic

Abstract **- Toroidal propellers have emerged as a promising low-noise propulsion solution for small unmanned aerial vehicles; however, their closed-loop geometry poses challenges for additive manufacturing quality control. This study investigates the geometric conformity of a toroidal propeller manufactured via Vat Photopolymerization (VPP), motivated by a systematic discrepancy between wind tunnel measurements and Computational Fluid Dynamics (CFD) predictions. The propeller was digitised using a Keyence VL-700 structured-light scanner and analysed against the digital model via Cloud-to-Mesh distance computation in CloudCompare after Iterative Closest Point registration. The global analysis reveals a mean deviation of +0.115 mm (standard deviation: 0.479 mm), with maximum positive and negative deviations of +1.531 mm and -1.163 mm. Segment-level analysis of the four blade surfaces reveals a pronounced inter-blade asymmetry, with mean deviations from +0.009 mm to +0.350 mm, attributed to the 3D printing orientation. The largest positive deviations are concentrated at the transition zones and trailing edges, where chord-relative deviations of 3-10 % alter local camber and angle of attack, partially explaining the experimental thrust exceeding CFD predictions. The findings confirm that VPP achieves acceptable accuracy for complex aerodynamic geometries, identifying printing orientation as a key factor and recommending process optimisation at the critical regions.**

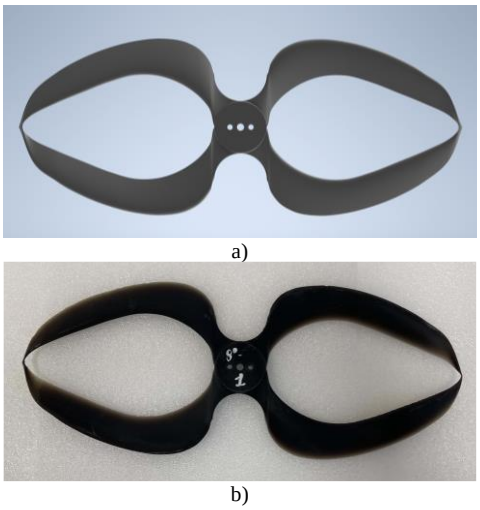
Keywords **- Toroidal propeller; UAV; Optical scanning; Geometric accuracy; VPP; CFD.**

1. INTRODUCTION

The rapid proliferation of multirotor Unmanned Aerial Vehicles (UAVs) across both civil and defence sectors has intensified demands on propulsion system performance, particularly with respect to acoustic emissions. Urban deployment scenarios require compliance with increasingly stringent noise regulations, while tactical military applications demand low acoustic signatures to minimise detection risk. In both contexts, the rotating propeller constitutes the dominant noise source, generating tonal components at blade passage frequency and its harmonics that propagate efficiently over distances relevant to operational use [1], [2]. Addressing this constraint without compromising thrust efficiency has become a central challenge in UAV propulsion engineering [2].

The toroidal propeller, introduced by researchers at MIT Lincoln Laboratory [3], offers a structurally distinctive response to this challenge. By curving each blade tip back towards the hub to form a continuous closed loop, the geometry fundamentally alters the tip vortex dynamics that underlie tonal noise generation in conventional open-blade designs. Rather than shedding discrete, concentrated tip vortices, the toroidal topology distributes vorticity continuously along the blade span, attenuating the dominant tonal components without requiring active noise control or significant thrust penalty [3], [4]. This characteristic has positioned the toroidal propeller as a compelling candidate for next-generation low-noise UAV propulsion [5].

Building on this premise, a dedicated experimental and numerical research programme was carried out at the Department of Aviation Technology, University of Defence, to characterise toroidal propeller performance under controlled laboratory conditions. Several propeller variants were designed and fabricated as part of this programme; the present study focuses on a two-bladed toroidal propeller based on the NACA 23012 airfoil, with a fixed blade angle of 8° and an outer diameter of 254 mm. The propeller was fabricated using Vat Photopolymerization (VPP) - a resin-based additive manufacturing process selected for its capacity to reproduce the complex closed-loop blade geometry with high surface fidelity. An initial study presented at the 2025 International Conference on Military Technologies confirmed measurably reduced tonal noise levels relative to a conventional propeller of equivalent diameter, validating the acoustic premise of the design [6].



a)

b)

Fig. 1. Toroidal propeller studied in this work: a) original CAD model; b) VPP-manufactured specimen.

During the aerodynamic evaluation phase, wind tunnel experiments and CFD simulations conducted in ANSYS Fluent revealed a systematic and persistent discrepancy

between measured and predicted thrust values. To investigate the possible contribution of manufacturing-induced geometric deviations to this discrepancy, an optical 3D scanning campaign was conducted using a Keyence VL-700 structured-light scanner, and the resulting scan was compared against the original CAD model using CloudCompare software.

This paper reports the methodology and findings of this geometric conformity assessment, discusses the implications of the identified deviations for the observed experimental-CFD discrepancy, and identifies directions for future work.

2. THEORETICAL AND METHODOLOGICAL BACKGROUND

A. Structured-Light Scanning and Cloud-to-Mesh Analysis

Structured-light 3D scanning is a non-contact surface measurement technique in which a known pattern of light is projected onto a target object and the resulting geometric distortion of the projected pattern is captured by one or more calibrated cameras to reconstruct the 3D surface geometry as a dense point cloud [7]. Unlike contact-based coordinate measurement machines, structured-light systems impose no mechanical load on the measured surface and can acquire complete surface geometry in a single automated scan cycle. Modern systems of this class are capable of achieving point resolutions in the micrometre range, making them particularly well-suited for the inspection of geometrically complex components such as toroidal propeller blades, where conventional measurement approaches are impractical due to the closed-loop topology [7], [8].

Quantitative comparison between a scanned surface and a reference CAD model is performed using the Cloud-to-Mesh (C2M) distance algorithm, as implemented in CloudCompare [9], an open-source software platform widely used in metrology, reverse engineering, and engineering inspection. The workflow proceeds in two stages. First, the scanned point cloud is registered to the CAD reference surface using the Iterative Closest Point (ICP) algorithm [10], which iteratively minimises the sum of squared distances between corresponding point pairs in the two datasets, eliminating residual positional and orientational offsets remaining after initial manual alignment. Second, the C2M algorithm computes the shortest signed distance from each point in the registered cloud to the nearest triangular face of the reference mesh, yielding a scalar field of signed deviations. Positive values indicate that the scanned surface protrudes beyond the nominal CAD geometry, while negative values indicate recession. The output comprises a colour-coded deviation map visualising the spatial distribution of deviations across the entire surface, together with a statistical distribution characterised by mean deviation, standard deviation, RMS, and maximum positive and negative values, from which manufacturing quality can be quantitatively assessed.

B. Geometric Accuracy of VPP-Manufactured Parts

VPP is a category of additive manufacturing that encompasses Stereolithography (SLA) and Digital Light Processing (DLP). It offers substantially higher dimensional accuracy and surface finish compared to extrusion-based methods such as Fused Filament Fabrication (FFF) [11]. Typical dimensional tolerances for VPP-printed parts fall within ±0.1-0.3 mm for features in the centimetre-to-decimetre scale, while surface roughness values of R_a = 1-4 μm are routinely achievable after post-curing. These characteristics make VPP a natural choice for manufacturing aerodynamic components where surface quality and geometric fidelity are critical to experimental validity [11], [12].

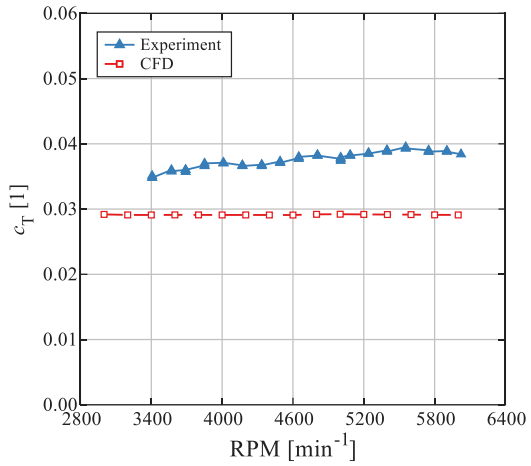
Despite these advantages, VPP parts are subject to several systematic sources of geometric deviation that become particularly significant for thin, highly curved geometries such as toroidal propeller blades. Photopolymer resin shrinkage during UV post-curing is amplified in regions of high local curvature and varying cross-sectional thickness. Layer-stepping artefacts arise at surfaces inclined at shallow angles to the build plane, producing a staircase approximation of smooth curved surfaces whose magnitude is governed by the layer thickness of the printing system. Additionally, support structure removal and surface post-processing may introduce localised irregularities that are not captured in the nominal CAD geometry. The spatial distribution of these deviation sources is inherently non-uniform: regions of high geometric complexity accumulate larger deviations, while flat or gently curved surfaces tend to remain close to the nominal dimensions. Understanding this distribution is essential for interpreting differences between experimentally measured and numerically predicted propeller performance, and motivates the segment-level analysis presented in Section IV [13].

3. DISCREPANCY BETWEEN EXPERIMENTAL AND CFD RESULTS

The aerodynamic performance of the propeller was evaluated through wind tunnel experiments and CFD simulations covering both static and dynamic operating conditions. The experimental campaign was carried out in the wind tunnel laboratory at the Department of Aviation Technology, University of Defence. Static thrust measurements were performed over a rotational speed range of approximately 3,400 to 6,000 min^{-1}, while dynamic measurements were conducted at two representative rotational speeds of 3,250 and 5,050 min^{-1} as a function of freestream airflow velocity. CFD simulations were performed in ANSYS Fluent using the Sliding Mesh approach with the *k-ε* turbulence model, with the propeller geometry defined by the nominal CAD model. Results are compared in terms of the thrust coefficient c_T, which normalises thrust with respect to air density, rotational speed, and propeller diameter, thereby eliminating the influence of ambient air density variations between experimental runs and enabling direct comparison with simulation data [14].

Under static conditions, the comparison of experimentally derived and CFD-predicted thrust coefficients as a function of rotational speed is shown in Fig. 2a. A clear and persistent gap between the two datasets is observed across the entire tested range. The experimentally derived c_T exhibits a slight upward trend with increasing rotational speed, suggesting a weak but measurable Reynolds number effect on the aerodynamic

loading of the blade. The CFD-predicted c_T, by contrast, remains essentially constant across the same range, which is consistent with the theoretical expectation that the thrust coefficient of a geometrically fixed propeller should be independent of rotational speed in idealised flow. The inability of the simulation to reproduce the experimentally observed trend points to limitations in the turbulence modelling at the low Reynolds numbers characteristic of this propeller class.



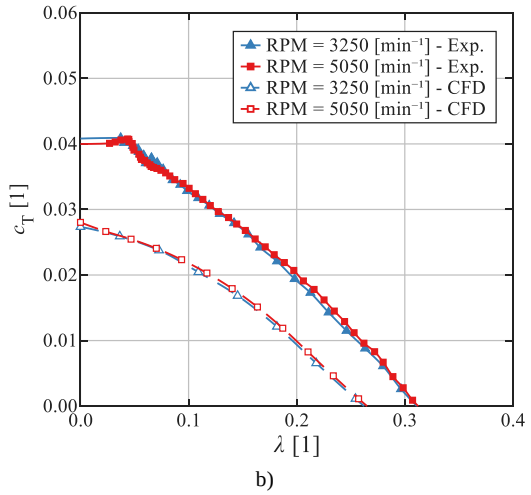


Fig. 2. Comparison of experimental and CFD-predicted thrust coefficients: a) static conditions; b) dynamic conditions.

Under dynamic conditions, the thrust coefficient as a function of advance ratio λ is presented in Fig. 2.b) for two representative rotational speeds. In both experiment and simulation, c_T decreases monotonically with increasing advance ratio, reflecting the progressive reduction in effective angle of attack as freestream velocity increases. In the experimental results, the two RPM curves are largely coincident but show a small and discernible separation at low advance ratios, consistent with a weak Reynolds number sensitivity at small effective angles of attack. Given the low blade angle of 8°, this behaviour is physically expected: the aerodynamic coefficients of the NACA 23012 section exhibit limited Reynolds number dependence at small incidence angles, so the inter-RPM difference remains modest. In the CFD results, the two curves coincide exactly across the full advance ratio range, indicating complete Reynolds number independence in the simulation. The discrepancy between experiment and simulation is most pronounced at low advance ratios and diminishes progressively as λ increases, with both datasets converging towards zero thrust at comparable advance ratios.

The consistent overestimation of c_T in the experiment relative to CFD, observed under both static and dynamic conditions, indicates that the source of discrepancy is structural rather than incidental. Two hypotheses are proposed to explain this behaviour. The first is that the CFD model underestimates aerodynamic loading due to turbulence modelling limitations at the low Reynolds numbers characteristic of this propeller, where laminar-to-turbulent transition and separation phenomena on the blade surface are not adequately captured by the *k-ε* formulation. The second is that the manufactured propeller geometry deviates from the nominal CAD design in a manner that increases effective blade loading beyond what simulations based on the ideal geometry can predict. The optical scanning study presented in the following section was conducted to quantitatively assess the validity of the second hypothesis.

4. OPTICAL 3D SCANNING, GEOMETRIC ANALYSIS AND DISCUSSION

A. Scanning Procedure

The optical 3D scanning was performed at the Department of Aviation Technology using a Keyence VL-700 structured-light scanner (Fig. 3). Prior to scanning, the propeller was thoroughly cleaned to remove particulate contamination. Due to the semi-glossy finish inherent to VPP photocured resin, a thin anti-reflective coating was applied uniformly to the blade surfaces to suppress specular reflection artefacts that could degrade point cloud quality. The scan was performed in fully automatic mode with a 360° angular coverage, combining five individual passes to ensure complete surface coverage, including the concave inner blade surfaces and the hub region. The total scan duration was approximately 10 minutes, yielding a mesh comprising 3,214,002 points and 1,071,334 triangular faces. After removal of duplicate vertices, 537,410 unique surface points were retained for analysis. The scanned mesh was exported as a binary STL file for compatibility with CloudCompare.



Fig. 3. Keyence VL-700 structured-light 3D scanner used for geometric conformity assessment.

B. CloudCompare Analysis

The scanned mesh was imported into CloudCompare and aligned to the original CAD model in two stages. In the first stage, a Point Pair Registration was performed by

manually selecting corresponding reference points on both models, establishing an initial rough alignment with an RMS of 0.519 mm. In the second stage, this alignment was refined using the Iterative Closest Point (ICP) algorithm, which iteratively minimises the sum of squared distances between the two surfaces until a convergence criterion of 1.0×10^{-7} mm is satisfied. The ICP registration converged to a final RMS of 0.482 mm computed on 50,000 points with a theoretical overlap of 100%, confirming reliable global alignment between the scanned and reference geometries.

Following registration, the Cloud-to-Mesh (C2M) distance was computed for all 537,410 surface points against the CAD reference mesh. Each point was assigned a signed scalar value representing the shortest distance to the nearest triangular face of the reference surface, with positive values indicating material excess relative to the nominal CAD geometry and negative values indicating material recession. The resulting scalar field was rendered as a false-colour deviation map spanning -1.163 mm (blue) to +1.531 mm (red), with the green band centred at zero deviation. The statistical parameters extracted from the full scalar field distribution are reported in Section IV.

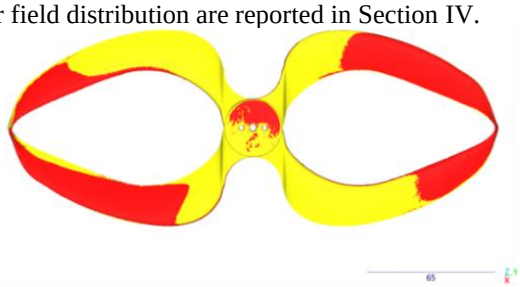
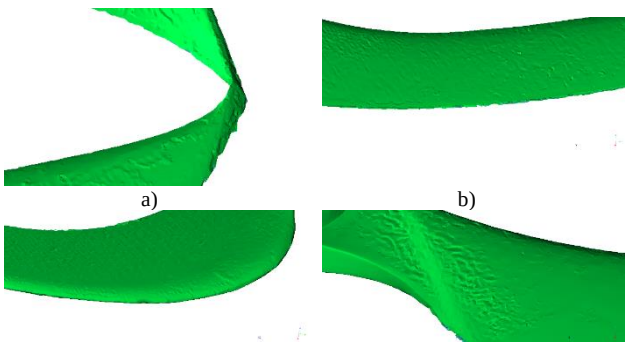


Fig. 4. Overlay of the registered scanned mesh (red) and the CAD reference model (yellow) in CloudCompare after ICP registration, upper surface view.

C. Results and Discussion

Visual Inspection of the Scanned Mesh

Prior to quantitative deviation analysis, a visual inspection of the scanned mesh was conducted by examining close-up views of geometrically complex regions that are inaccessible to direct tactile or visual assessment on the physical propeller. The high spatial resolution of the Keyence VL-700 scanner, combined with the dense mesh representation in CloudCompare, enables surface features at the sub-millimetre scale to be observed and documented in a manner that would not be possible through conventional manual inspection.



a) b) c) d)

Fig. 5. Close-up views of the scanned mesh revealing manufacturing-induced surface imperfections: a) transition zone, b) trailing edge, c) leading edge, d) blade surface.

Global Deviation Map and Statistical Distribution

The deviation maps of the upper and lower surfaces obtained from the C2M analysis are presented in Fig. 6. The colour scale spans from -1.163 mm (blue) to +1.531 mm (red), with green corresponding to deviations near zero, and is held constant across all deviation map figures in this study to allow direct visual comparison between surfaces and segments.

The upper surface exhibits a pronounced spatial gradient from the hub region towards the blade trailing edges and transition zones. Positive deviations, represented by yellow to red colouring, increase progressively in regions of greater blade curvature, while the hub and the inner blade body remain predominantly green, indicating deviations close to zero. The lower surface presents a contrasting pattern: negative deviations (blue to green) dominate over much of the blade area, with positive deviations appearing only at localised regions near the trailing edges and transition zones. This systematic asymmetry between the upper and lower surfaces is physically consistent with the VPP printing orientation, in which the suction-side geometry is more exposed to differential resin shrinkage and layer-stepping effects during curing, while the pressure side experiences different curing conditions due to its proximity to the build platform.

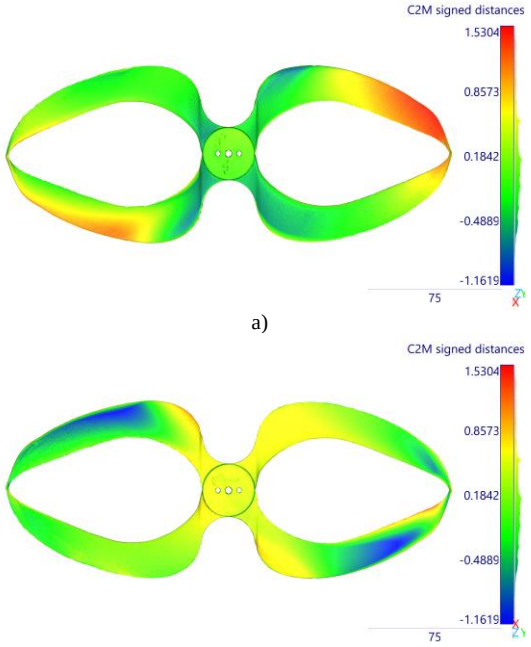


Fig. 6. C2M deviation maps: a) upper surface; b) lower surface.

The statistical distribution of the signed C2M deviations is presented in Fig. 7, showing both the Gaussian and Weibull fits to the histogram data.

The Weibull distribution provides a superior fit, as confirmed by its lower χ^2 distance relative to the Gaussian approximation, which is consistent with the right-skewed character of the distribution visible in the histogram. The positive mean deviation μ of +0.115 mm represents a statistically significant systematic positive bias. Although modest in absolute terms, this value indicates that the VPP manufacturing process introduces a consistent and reproducible geometric offset - material excess relative to the CAD nominal geometry - rather than random scatter.

The narrow 95% confidence interval of ±0.001 mm, derived from 537,410 measurement points, confirms the statistical robustness of this finding. At the trailing edges and transition zones, where deviations reach up to +1.531 mm, the relative deviation with respect to local chord length becomes 3-10% (estimated based on a local chord length of 15-20 mm in these regions), a geometrically significant perturbation at the low Reynolds numbers characteristic of this propeller, where even modest changes in local camber and effective angle of attack can produce disproportionate changes in aerodynamic force coefficients.

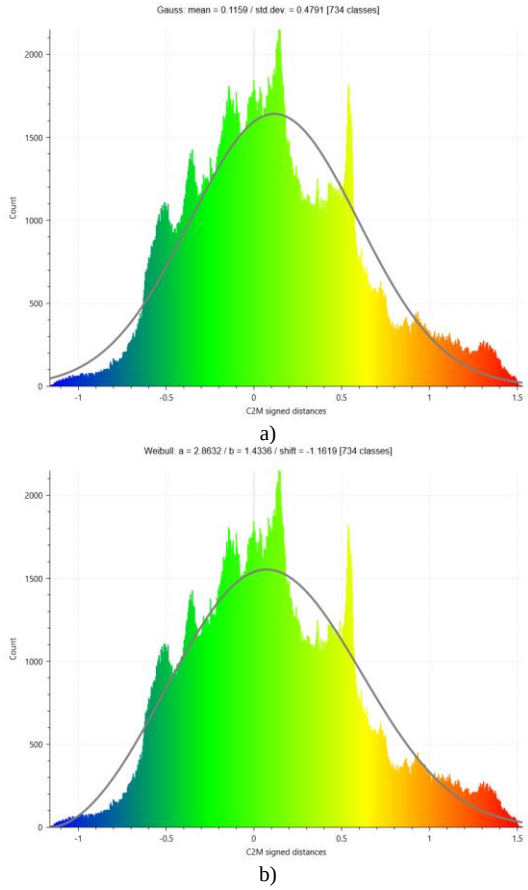


Fig. 7. C2M signed distance distributions: a) Gaussian fit; b) Weibull fit.

The right-skewed distribution, better described by the Weibull fit, reflects the physical reality that the majority of the blade surface achieves good dimensional accuracy within the green zone of the deviation map, while a minority of localised regions accumulate significantly larger positive deviations. These regions, attributable to differential resin shrinkage during UV post-curing and layer-stepping artefacts at surfaces inclined at shallow angles to the build plane, are the primary contributors to the experimentally observed thrust exceeding CFD predictions based on the nominal CAD geometry.

Segment Analysis

To investigate the spatial distribution of geometric deviations in greater detail, the scanned model was divided into five segments: the hub region and four blade segments. The four blade segments were numbered clockwise starting from the upper-right half, such that Blade-segments 1 and 2 together form the right-hand blade and Blade-segments 3 and 4 the left-hand blade. For each segment, the C2M deviation map and the corresponding histogram are presented, and the key parameters are summarised in Table 1. A Weibull fit is shown for a visual consistency, but the segment parameters are computed directly as descriptive statistics and the modality is read from the histogram itself; for the multimodal segments, the poor fit merely reflects the spatial heterogeneity of the deviations.

The hub segment exhibits predominantly green colouring in its deviation map (Fig. 8), indicating that the majority of its surface deviates by less than ±0.2 mm from the CAD reference, confirming that the hub is the most dimensionally accurate region of the propeller, with a standard deviation of only 0.252 mm. However, the histogram reveals a distinctly bimodal distribution with two identifiable peaks: one centred near zero, corresponding to the flat central surface, and a second at approximately +0.45 mm, corresponding to the rim and peripheral regions. This bimodal character reflects the geometric complexity of the hub boundary and the concentration of resin at the rim during post-curing. The lower surface of the hub exhibits systematically higher positive deviations compared to the upper surface, likely attributable to resin accumulation at the build platform interface during VPP printing.

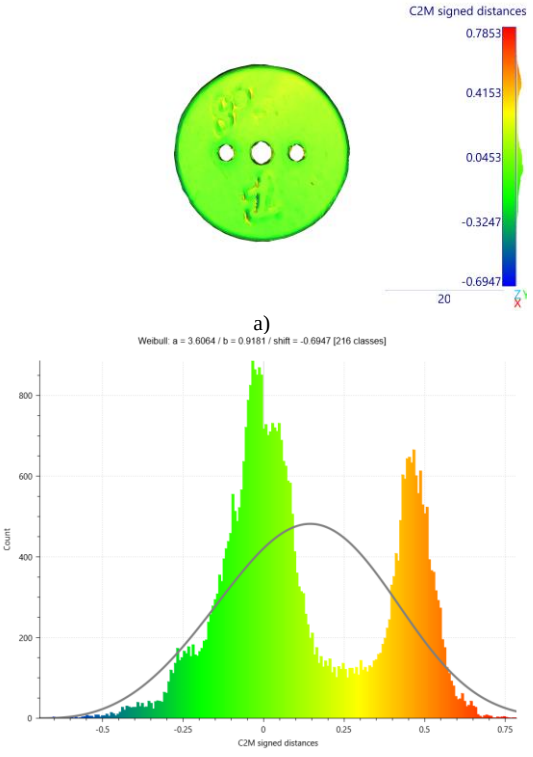
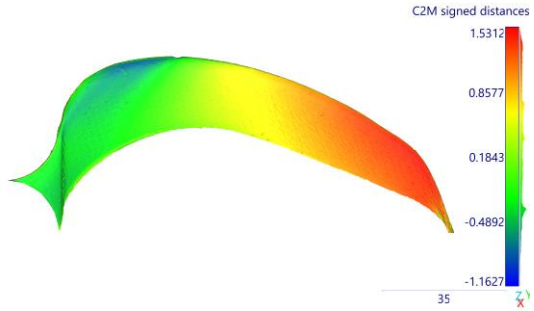


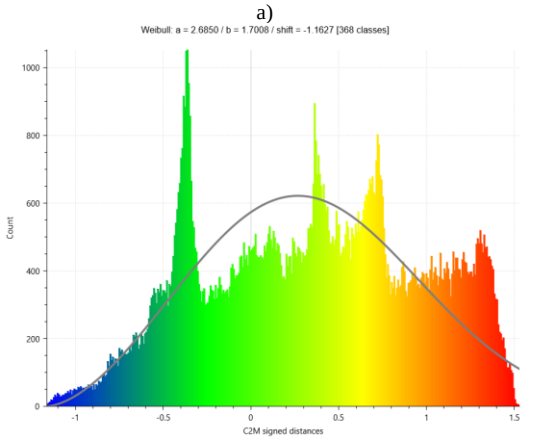
Fig. 8. Hub segment: a) deviation map; b) deviation histogram with Weibull fit.

Blade-segment 1 exhibits the largest geometric deviations of all blade-segments, with a mean deviation of +0.350 mm and a standard deviation of 0.616 mm (Fig. 9). The deviation map shows a clear spatial gradient from the blade root, which remains near zero, towards the transition zone and trailing edge, where deviations reach up to +1.531 mm. The histogram spans the full deviation range and is strongly multimodal, with several sharp peaks superimposed on a broad background. The poor quality of both Gaussian and Weibull fits is itself informative,

indicating that the deviation field on Blade-segment 1 does not follow any simple parametric distribution and is instead the superposition of contributions from multiple aerodynamic sub-regions with distinct deviation characteristics.



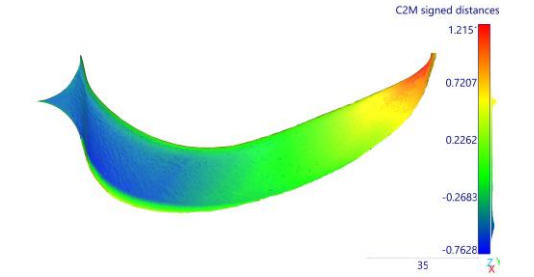
a)



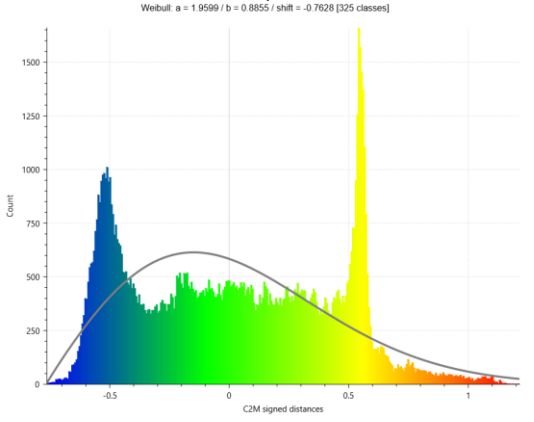
b)

Fig. 9. Blade-segment 1: a) deviation map; b) deviation histogram with Weibull fit.

Blade-segment 2 presents a strikingly different pattern compared to Blade-segment 1, with a mean deviation of only +0.022 mm (Fig. 10).



a)

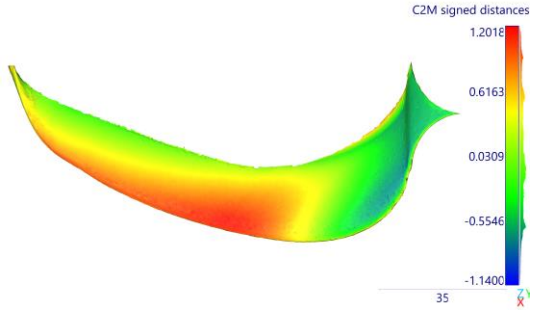


b)

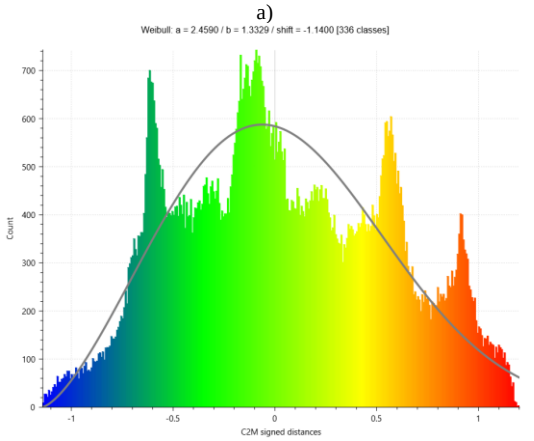
Fig. 10. Blade-segment 2: a) deviation map; b) deviation histogram with Weibull fit.

The deviation map reveals a pronounced spatial asymmetry: the root-side portion is dominated by negative deviations reaching -0.763 mm, while the transition zone exhibits positive deviations reaching +1.215 mm. The histogram is clearly bimodal, with two distinct peaks reflecting these two opposing regions. The near-zero global mean results from the partial cancellation of these opposing regions. As the lower half of the same right-hand toroidal blade as Blade-segment 1, Blade-segment 2 occupies a different build orientation, so that deviations of opposite sign accumulate along its arc - negative near the root and positive at the transition - in contrast to the predominantly positive deviations of the upper half.

Blade-segment 3 shows a similar global mean to Blade-segment 2 (+0.043 mm), but with a different spatial arrangement (Fig. 11). The leading-edge half of the blade is dominated by large positive deviations of up to +1.201 mm, while the transition zone side remains close to zero. The histogram is clearly multimodal, with several distinct peaks reflecting the spatially heterogeneous deviation field across this segment. The standard deviation of 0.516 mm is the second largest among all segments, indicating a high degree of spatial variability in the deviation field.



a)



b)

Fig. 11. Blade-segment 3: a) deviation map; b) deviation histogram with Weibull fit.

Blade-segment 4 is the most geometrically accurate of all four blade-segments, with a mean deviation of +0.009 mm and a standard deviation of 0.271 mm (Fig. 12). The deviation map shows predominantly green colouring across the blade body, with minor positive deviations at the leading edge and a localised negative region at the transition zone. The histogram approximates a unimodal distribution centred near zero, making Blade-segment 4 the only segment for which the parametric fit is reasonably representative of the data. The comparatively superior accuracy of Blade-segment 4 is attributed to its more favourable printing orientation, with fewer overhanging

surfaces and reduced support structure requirements during fabrication.

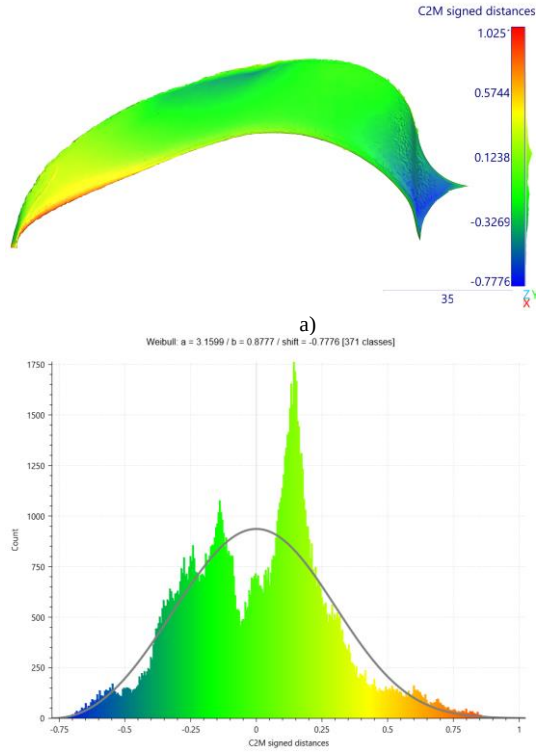


Fig. 12. Blade-segment 4: a) deviation map; b) deviation histogram with Weibull fit.

The segment statistics in Table 1 reveal asymmetry at two levels. Within the right-hand blade, the upper half (Blade-segment 1, +0.350 mm) deviates far more than the lower half (Blade-segment 2, +0.022 mm); across the rotor, the asymmetry is driven primarily by Blade-segment 1, whose mean exceeds that of the next-largest segment by a factor of eight while the remaining three segments cluster within +0.009 mm to +0.043 mm. Both reflect the print orientation, through which each half-loop and each blade experienced different build angles and support configurations.

TABLE I. Statistical summary of C2M deviations per segment.

Segment	Mean [mm]	Std.dev. [mm]	Max^+ [mm]	Max^- [mm]	Distribution type
Total	+0.115	0.479	+1.531	-1.163	Right-skewed
Hub	+0.131	0.252	+0.785	-0.695	Bimodal
Blade-segment 1	+0.350	0.616	+1.531	-1.163	Multimodal
Blade-segment 2	+0.022	0.418	+1.215	-0.763	Bimodal
Blade-segment 3	+0.043	0.516	+1.201	-1.140	Multimodal
Blade-segment 4	+0.009	0.271	+1.025	-0.778	Near-unimodal

4) Local Geometric Roughness

In addition to the global and segment-level deviation analysis, the local geometric roughness of the scanned surface was computed using the geometric features tool in CloudCompare with a neighbourhood radius of 1.0 mm. For each surface point, the roughness value is defined as the distance from that point to the best-fit plane computed from its local neighbourhood, thereby quantifying sub-millimetre surface irregularities at the scale of individual VPP layers. This metric captures a complementary aspect of manufacturing quality that is not reflected in the C2M deviation analysis: whereas the deviation map describes systematic dimensional offset relative to the CAD reference, the roughness map characterises local surface texture arising from the layer-by-layer nature of the printing process. The roughness maps of the upper and lower surfaces are presented in Fig. 13, and the statistical distribution is shown in Fig. 14. The colour scale spans from 0 (blue, smooth) to 0.616 mm (red, rough). The Weibull model was selected for distribution fitting for the same reason as in the segment analysis: the roughness distribution is strongly right-skewed and bounded below by zero, making it fundamentally incompatible with the symmetric Gaussian model. The Weibull distribution with a shape parameter a = 0.716, which is less than unity, describes a monotonically decreasing distribution, confirming that the vast majority of surface points exhibit very low roughness values, with only a small fraction of points concentrated at the leading and trailing edges reaching elevated roughness levels.

The roughness maps reveal a spatial pattern that is markedly different from and complementary to the C2M deviation maps. The blade body is dominated by deep blue colouring, indicating local roughness values below 0.05 mm, consistent with the smooth surface finish expected from VPP technology. By contrast, the leading edges, trailing edges, and transition zones are characterised by elevated roughness values shown in green, yellow, and localised red, reaching up to 0.616 mm. This pattern reflects two distinct physical mechanisms. At the trailing and leading edges, the thin cross-sections and high local curvature amplify the layer-stepping effect, producing a serrated edge profile as observed in visual inspection. At the transition zones, the abrupt change in blade curvature creates favourable conditions for resin accumulation and localised surface irregularities during post-curing.

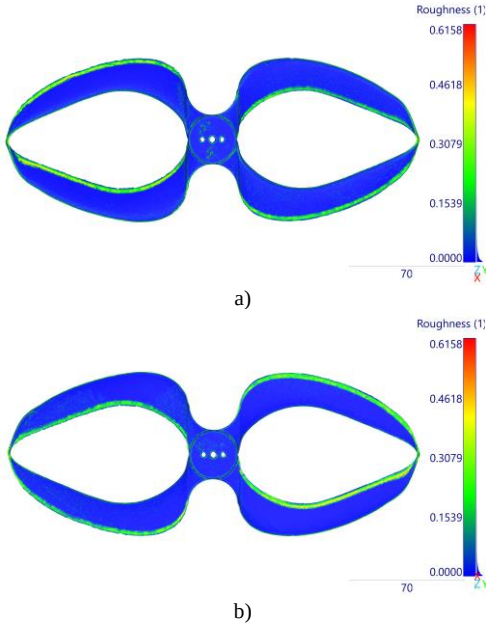


Fig. 13. Local geometric roughness maps: a) upper surface; b) lower surface.

The mean roughness of 61 µm across the full surface is consistent with the 50 µm layer thickness of the VPP system and can be understood as a measure of the average layer-stepping amplitude at the surface. It should be noted that this metric represents local 3D geometric irregularity computed over a 1.0 mm neighbourhood radius and is not directly equivalent to the ISO-standardised surface roughness parameter R_a, which is defined along a one-dimensional profile at a much finer scale. The two metrics are therefore not numerically comparable, and the roughness values reported here should be interpreted as a mesoscale surface texture indicator rather than a conventional surface finish parameter.

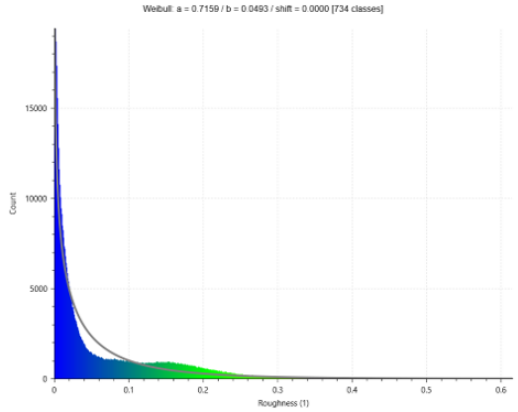


Fig. 14. Local geometric roughness distribution with Weibull fit.

5) Implications for the Experimental-CFD Discrepancy

The geometric deviation analysis presented in this section provides a physically consistent partial explanation for the systematic discrepancy between experimental and CFD thrust coefficients reported in Section III. The positive deviations concentrated at the blade transition zones and trailing edges, particularly pronounced on Blade-segment 1 with a mean deviation of +0.350 mm, correspond to localised increases in effective blade camber and angle of attack relative to the nominal CAD geometry. These changes increase the aerodynamic loading of the affected blade sections beyond what CFD simulations based on the ideal geometry can predict, contributing directly to the experimentally observed overestimation of c_T.

The inter-segment asymmetry identified in the segment analysis introduces a further complication: the four blade segments exhibit substantially different deviation characteristics, implying that the manufactured propeller does not possess the rotational symmetry assumed in the CFD model. This asymmetry introduces aerodynamic imbalance across the rotor disk that is absent from the simulation, and may account for part of the scatter observed in experimental measurements at equivalent rotational speeds.

It should be acknowledged, however, that geometric deviations alone are unlikely to fully account for the observed discrepancy. As noted in Section III, the k-ε turbulence model does not resolve laminar-to-turbulent transition at the low Reynolds numbers characteristic of this propeller, which independently contributes to thrust underestimation in CFD. Isolating the respective contributions of geometric deviation and turbulence modelling to the total discrepancy will require CFD re-simulation using the as-scanned geometry as the computational domain, which is identified as the primary direction for future work.

5. V. CONCLUSION

This paper has presented a comprehensive geometric conformity assessment of a toroidal propeller manufactured using Vat Photopolymerization, motivated by a systematic discrepancy between wind tunnel experimental thrust coefficients and CFD predictions obtained in ANSYS Fluent. Optical 3D scanning was performed using a Keyence VL-700 structured-light scanner, and the resulting mesh of 537,410 surface points was compared against the original CAD model via Cloud-to-Mesh distance analysis in CloudCompare following ICP registration.

Visual inspection of the scanned mesh revealed manufacturing-induced surface imperfections at the trailing edges, leading edges, transition zones, and blade body that are imperceptible to the naked eye and undetectable by touch on the finished part. These include edge serrations, faceted geometry at the transition zones, and layer-stepping artefacts on the blade body surface, all of which are characteristic of the VPP layer-by-layer deposition process.

The global C2M analysis confirms a systematic positive bias of +0.115 mm in mean surface deviation, with the most pronounced positive deviations concentrated at the blade transition zones and trailing edges, reaching up to +1.531 mm locally. The deviation distribution is better described by a Weibull model than a Gaussian approximation, reflecting the right-skewed, spatially non-uniform character of the manufacturing deviations. Segment-level analysis reveals a striking inter-segment asymmetry: mean deviations range from +0.009 mm on the most accurate blade segment to +0.350 mm on the least accurate, a difference attributable to the printing orientation and its effect on support structure distribution and curing conditions across different blade surfaces. Complementary roughness analysis confirms that the blade body achieves low surface irregularity consistent with VPP capabilities, while elevated roughness is localised at the leading and trailing edges, consistent with the visual inspection findings.

These geometric deviations provide a physically consistent partial explanation for the experimental-CFD thrust discrepancy. Localised increases in effective blade camber and angle of attack at the transition zones and trailing edges increase aerodynamic loading beyond what simulations based on the nominal geometry predict, while the inter-blade asymmetry introduces additional aerodynamic imbalance absent from the CFD model, the right-hand blade carrying a markedly less accurate upper half. Turbulence modelling limitations of the k-ε formulation at low Reynolds numbers are identified as a concurrent contributing factor that cannot be excluded.

Two directions for future work are proposed. The first is optimisation of VPP process parameters, particularly print orientation, support strategy, and post-cure conditions, to reduce systematic deviations at the aerodynamically critical transition zones and trailing edges, and to improve inter-blade geometric consistency. The second is CFD re-simulation of the propeller using the as-scanned geometry

as the computational domain, which would allow the respective contributions of geometric manufacturing deviations and turbulence modelling assumptions to the total thrust discrepancy to be systematically isolated and quantified.

Acknowledgment

This study was supported by the University of Defence, Brno, Czech Republic (Scientific project SV26-206/1).

References

[1] G. Sinibaldi and L. Marino, "Experimental analysis on the noise of propellers for small UAV," *Appl. Acoust.*, vol. 74, no. 1, pp. 79–88, 2013, doi: 10.1016/j.apacoust.2012.06.011.

[2] P. Candeloro, D. Ragni, and T. Pagliaroli, "Small-Scale Rotor Aeroacoustics for Drone Propulsion: A Review of Noise Sources and Control Strategies," *Fluids*, vol. 7, no. 8, p. 279, Aug. 2022, doi: 10.3390/fluids7080279.

[3] MIT Lincoln Laboratory, "Toroidal Propeller," Massachusetts Institute of Technology, Massachusetts, online, 2022. Accessed: Dec. 22, 2024. [Online]. Available: https://www.ll.mit.edu/sites/default/files/other/doc/2022-09/TVO_Technology_Highlight_41_Toroidal_Propeller.pdf

[4] W. Wei, Y. Ma, S. Wei, D. Wang, M. Guo, and Q. Yan, "Analysis and Evaluation of Aerodynamic Noise Characteristics of Toroidal Propeller," *Drones*, vol. 8, no. 12, p. 753, Dec. 2024, doi: 10.3390/drones8120753.

[5] J. Sun, K. Yonezawa, E. Shima, and H. Liu, "Integrated Evaluation of the Aeroacoustics and Psychoacoustics of a Single Propeller," *Int. J. Environ. Res. Public. Health*, vol. 20, no. 3, p. 1955, Jan. 2023, doi: 10.3390/ijerph20031955.

[6] V. D. Pham and D. Rozehnal, "Acoustic Measurements of UAV Propulsion System with Toroidal Propellers," in *2025 International Conference on Military Technologies (ICMT)*, Brno, Czech Republic, May 2025, pp. 1–6. doi: 10.1109/ICMT65201.2025.11061273.

[7] J. Geng, "Structured-light 3D surface imaging: a tutorial," *Adv. Opt. Photonics*, vol. 3, no. 2, p. 128, Jun. 2011, doi: 10.1364/AOP.3.000128.

[8] J. Salvi, J. Pagès, and J. Batlle, "Pattern codification strategies in structured light systems," *Pattern Recognit.*, vol. 37, no. 4, pp. 827–849, Apr. 2004, doi: 10.1016/j.patcog.2003.10.002.

[9] D. Girardeau-Montaut, "CloudCompare: 3D Point Cloud and Mesh Processing Software," Open Source Project. [Online]. Available: https://www.cloudcompare.org

[10] P. J. Besl and N. D. McKay, "A method for registration of 3-D shapes," *IEEE Trans. Pattern Anal. Mach. Intell.*, vol. 14, no. 2, pp. 239–256, Feb. 1992, doi: 10.1109/34.121791.

[11] M. Pagac *et al.*, "A Review of Vat Photopolymerization Technology: Materials, Applications, Challenges, and Future Trends of 3D Printing," *Polymers*, vol. 13, no. 4, p. 598, Feb. 2021, doi: 10.3390/polym13040598.

[12] N. Badanova, A. Perveen, and D. Talamona, "Study of SLA Printing Parameters Affecting the Dimensional Accuracy of the Pattern and Casting in Rapid Investment Casting," *J. Manuf. Mater. Process.*, vol. 6, no. 5, p. 109, Sep. 2022, doi: 10.3390/jmmp6050109.

[13] A. Kalilayeva, D. Zhumashev, D. Wei, A. Perveen, and D. Talamona, "Investigation of Stereolithography Additively Manufactured Components for Deviations in Dimensional and Geometrical Features," *Polymers*, vol. 16, no. 23, p. 3311, Nov. 2024, doi: 10.3390/polym16233311.

[14] V. D. Pham and D. Rozehnal, "Study of Toroidal Propellers with Reduced Acoustic Signature," in *23rd International Scientific Conference "Measurement, Diagnostics, and Dependability of Aircraft Systems,"* Brno, Czech Republic: University of Defence, 2025, pp. 120–127.